Journal of
Materials Chemistry A

ROYAL SOCIETY
OF CHEMISTRY

PAPER

View Article Online
View Journal | View Issue

Check for updates

Cite this: *J. Mater. Chem. A*, 2025, **13**, 35533

A band-aid-based $MoSe_2/Nb_2C$ wearable supercapacitor for integrated ammonium-ion energy storage and real-time pressure monitoring

Kaaviah Manoharan[a] and Martin Pumera *[abc]

The market for wearable electronic devices is rapidly growing, with increasing potential for future development. Researchers around the globe are striving to enhance these devices, focusing on achieving a balance between functionality and wearability to drive commercialization. Supercapacitors are regarded as one of the most promising energy storage technologies, bridging the gap between conventional batteries and dielectric capacitors to support high-power applications. This study presents the hybrid supercapacitor application of molybdenum sulfide, molybdenum selenide, and niobium carbide on band-aid-based wearable electrodes tested in three different electrolytes (sodium sulfate, ammonium sulfate, and zinc sulfate). Among the three electrolytes, the ammonium sulfate electrolyte exhibited exceptional electrochemical performance, including high specific capacitance, excellent power density, and remarkable cycling stability. Band-aid-based wearable ammonium ion hybrid supercapacitors were designed to explore their real-time applicability, utilizing activated carbon as the negative electrode and molybdenum selenide/niobium carbide as the positive electrode. The fabricated ammonium ion hybrid supercapacitor offers a maximum specific capacitance of 120 F g^{-1} with 92% capacitance retention after 20 000 cycles. Also, it exhibits an outstanding energy density and power density. This suggested multipurpose integrated system opens new possibilities for creating flexible and adaptive wearable electronics. A glucose sensor is shown to be powered by the fabricated ammonium ion hybrid supercapacitor. The molybdenum selenide/niobium carbide-coated band-aid is also sandwiched between tiny layers of copper foil to create a pressure sensor. It is powered by an ammonium ion hybrid supercapacitor, which enables precise and steady real-time monitoring of the radial pulse pressure on the wrist of a person. This work creates new opportunities to explore the potential of wearable technology and nanomaterials to develop self-sufficient, cost-effective healthcare systems for monitoring health parameters in real-time.

Received 30th July 2025
Accepted 1st September 2025

DOI: 10.1039/d5ta06175j

rsc.li/materials-a

1 Introduction

The severe environmental degradation brought on by greenhouse gas emissions from burning fossil fuels necessitates the advancement of energy storage and conversion technologies. Because of their portability and great energy density, batteries—particularly lithium-ion batteries—can meet the demands of the modern world.[1,2] However, the current battery technologies' limited power density restricts their wider range of applications. In contrast, supercapacitors are a possible substitute for traditional batteries since they provide a far higher power density. Electric double-layer capacitors (EDLCs) and pseudocapacitors are two varieties of supercapacitors that differ in how they store charge. EDLCs are often based on carbonaceous substances that store charge at the interface between the electrode and electrolyte through electrostatic.[3] Meanwhile, conducting polymers and transition metal oxides are examples of pseudocapacitive electrode materials.[4] The reversible faradaic redox mechanisms that underlie pseudocapacitors generally offer higher specific capacitance and energy density than EDLCs.[5,6] However, it is also important to mention that batteries currently offer a higher energy density than supercapacitors. Therefore, creating new electrode materials for supercapacitors is essential to boosting their energy density.

Active materials in wearable technology are crucial for achieving sensing, along with energy storage devices. These devices should continue to perform as intended even when subjected to various human motions. However, energy storage devices and sensors operate in entirely different ways, so it is typically necessary to use separate device architectures made of

---

[a] *Future Energy and Innovation Laboratory, Central European Institute of Technology, Brno University of Technology, Purkyňova 123, 61200 Brno, Czech Republic. E-mail: martin.pumera@ceitec.vtbr.cz*

[b] *Faculty of Electrical Engineering and Computer Science, VSB – Technical University of Ostrava, 17. listopadu 2172/15, 70800 Ostrava, Czech Republic*

[c] *Department of Medical Research, China Medical University Hospital, China Medical University, No. 91 Hsueh-Shih Road, Taichung 40402, Taiwan*

other materials using various fabrication techniques.[7] This makes it challenging, time-consuming, and limits manufacturing scalability because sensors and energy storage devices are frequently made separately before being assembled on the same substrate. Thus, it is crucial and urgently necessary to develop a straightforward and scalable process for producing active materials that may be utilized for energy storage and sensing in wearable electronics.[8,9] Paper,[10] textiles,[11] band-aids,[12] and other flexible materials have emerged as the most viable recyclable substrates for energy applications in recent years. For instance, supercapacitors,[13] solar cells,[14] and micro-supercapacitors[15] have all made extensive use of certain band-aid-based components. Because they are reasonably priced, highly breathable, and easy to wear, band-aids made of textile fabric and a cotton pad can be used as a substrate for wearable technology.[12] Meanwhile, scientists have created several extremely effective materials for energy storage devices. Layered transition metal dichalcogenides are currently receiving much attention in energy-related applications because of their low cost, strong catalytic activity, and great chemical stability.[16] Because two-dimensional (2D) materials have large surface areas and sheet-like morphology that enhance the exposure of active regions, they are being thoroughly studied for use in supercapacitor electrodes.[17] For high-performance supercapacitor electrodes, the 2D transition metal carbides and nitrides ($M_{n+1}X_nT_x$), also known as MXenes, have been extensively studied because of their remarkable electrical conductivity, abundance of active sites, and fascinating lamellar structures.[18] 2D Nb_2C MXenes display the best performance and very good cycle performance. Unfortunately, their relatively low specific capacitance still limits the actual applications of MXene-based electrode materials. To overcome the drawbacks of Nb_2C MXenes, compositing the material with pseudocapacitive materials is a crucial tactic frequently employed to increase the capacitance of Nb_2C MXene-based supercapacitors.[19] In this study, multilayer Nb_2C MXenes were employed without further delamination into single/few-layer nanosheets.[20]

Numerous studies have been conducted on pseudocapacitive materials, such as transition metal selenides, oxides, and sulfides, owing to their remarkable electrochemical performance and theoretical capacitance. An MX_2 structure is produced in 2D transition metal dichalcogenides (TMDs) when a metal layer (M = Mo) is sandwiched between two chalcogen layers (X = S and Se). Because of its layered structure, weak van der Waals interactions between the layers, and several characteristics, molybdenum disulfide (MoS_2) and molybdenum diselenide ($MoSe_2$) have dragged the interest of researchers.[21] The hexagonal structures of the layered TMDs MoS_2 and $MoSe_2$ are composed of molybdenum atoms stacked among two chalcogen layers (S and Se) by weak van der Waals interactions.[22] We created a layered structure by fusing Nb_2C with MoS_2 and $MoSe_2$ nanosheets to improve capacitance performance. To ensure more active sites for redox reactions, the two distinct (Nb_2C/MoS_2 and $Nb_2C/MoSe_2$) nanocomposites are assumed to prevent MXenes or MoS_2 and $MoSe_2$ nanosheets from aggregating. Additionally, this structure guarantees robust interaction between the constituents, which is advantageous for preserving excellent electrical and mechanical contact. Motivated by these goals, it is highly likely that the hybrids of Nb_2C-MXenes (a high conductivity material) and MoS_2 and $MoSe_2$ (a pseudocapacitive material) can combine their benefits to improve electrochemical performance. In recent years, MXene/TMD heterostructures have attracted increasing attention because they combine the high electrical conductivity of MXenes with the layered structure and pseudocapacitance of

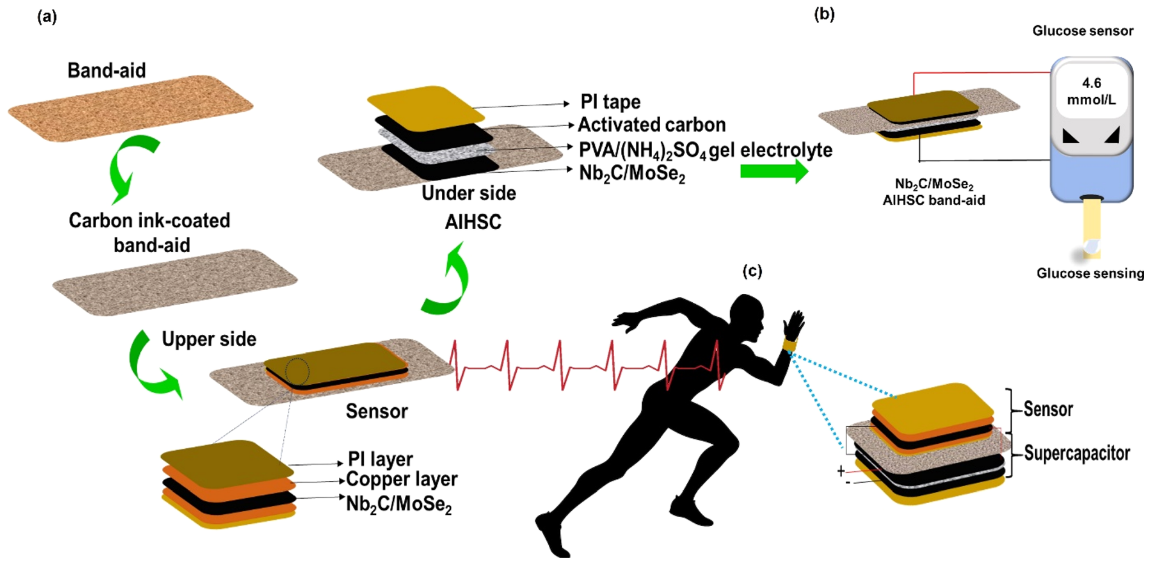

Scheme 1 Real-time bio monitoring applications of an integrated wearable band-aid based $Nb_2C/MoSe_2\|AC$ ammonium ion hybrid supercapacitor flexible device: (a) schematic illustration of the $Cu/Nb_2C/MoSe_2/Cu$ flexible sensor and $Nb_2C/MoSe_2\|AC$ ammonium ion hybrid supercapacitor flexible device fabrication. (b) Fabricated ammonium ion hybrid supercapacitor powering a glucose sensor and (c) fabricated pressure sensor powered by an ammonium ion hybrid supercapacitor for real-time radial pulse monitoring.

TMDs. Such hybrids can suppress MXene restacking, provide additional redox-active sites, and facilitate rapid ion transport. Importantly, previous reports have demonstrated that the capacitance of MXene heterostructure electrodes can exceed that of the individual components, confirming the presence of strong synergistic effects.[23,24] This motivates the design of Nb_2C/MoS_2 and Nb_2C/$MoSe_2$ composites in our work, where Nb_2C provides high conductivity and structural stability, while MoS_2 and $MoSe_2$ contribute interlayer ion storage and pseudocapacitive charge transfer.

These days, metal ions are used as charge carriers in the majority of electrochemical energy storage devices, including Li-ion batteries, Zn-ion batteries, and Na-ion batteries.[25] The lack of innovative nonmetal-ion electrochemical capacitors and batteries is due to the contempt for nonmetal cation charge carriers. Various characteristics set NH_4^+ apart from metal ions such as Na^+, Mg^{2+}, and Zn^{2+}. Because NH_4^+ has the lightest molar mass of 18 g mol^{-1} and the lowest hydrated ionic size among aqueous electrolytes, it may diffuse quickly. Interest in the unique properties of NH_4^+ has increased ever since the growth of the "shaking chair" ammonium-ion battery (AIB).[26] Most research on NH_4^+ charge carriers has been restricted to batteries and has focused mostly on creating appropriate host materials for NH_4^+ storage and investigating the related chemistry. Other NH_4^+ charge carrier-based rechargeable energy storage technologies have not been developed, particularly for hybrid supercapacitors.[27,28] Compared to commonly used cations such as Na^+, K^+, or H^+ in acidic electrolytes, NH_4^+ offers unique advantages for flexible supercapacitors. Its small hydrated radius allows faster ion diffusion and higher ionic conductivity, contributing to enhanced power density. In addition, NH_4^+ can form hydrogen-bonding interactions with the electrode surface and exhibits proton-like pseudocapacitance, thereby improving charge storage and energy density. These reversible interactions also contribute to superior cycling stability, as evidenced by 92% capacitance retention after 20 000 cycles in our device. Importantly, $(NH_4)_2SO_4$ is a neutral, biocompatible electrolyte, which makes it safe for skin-contact applications and highly suitable for integration into flexible, wearable band-aid platforms.

As illustrated in Scheme 1, using an ammonium ion hybrid supercapacitor, we created a multipurpose smart band-aid with applications for health monitoring and sensing. The band-aid's woven fabric is coated with carbon ink, and then the two active materials (Nb_2C/$MoSe_2$ and Nb_2C/MoS_2) are produced and applied. The doctor blade method is adopted to create flexible electrodes. MoS_2 and $MoSe_2$ are layered transition metal dichalcogenides (TMDs) with the layered structure that allows for ion intercalation between layers, making them promising candidates for energy storage. $MoSe_2$ has a larger interlayer spacing and higher electrical conductivity compared to MoS_2, which can facilitate faster ion and electron transport. Conductive carbon is added to the electrode composite to improve overall electrical conductivity and support efficient charge transfer during electrochemical cycling. Smart wearable band-aid opens up a new path for the growth of multipurpose integrated band-aid-based wearable electronics, which have great promise for applications including health monitoring. More significantly, the prototype supercapacitor demonstrated its immense potential for wearable technology by powering a flexible, self-powered integrated pressure sensor that could be directly attached to the human body to detect motions.

Herein, we present a band-aid-based wearable ammonium-ion hybrid supercapacitor (AIHSC) that combines innovations at both the material and device levels. At the materials level, the Nb_2C/$MoSe_2$ composite electrode leverages the high conductivity of MXenes and the redox activity with enlarged interlayer spacing of $MoSe_2$, thereby providing enhanced ion transport, high specific capacitance, and excellent long-term cycling stability compared to conventional Nb_2C/MoS_2 and pristine MXene electrodes. At the device level, this work demonstrates for the first time a flexible, band-aid-integrated AIHSC employing NH_4^+ ions as charge carriers. The small hydrated radius and proton-like pseudocapacitance of NH_4^+ contribute to superior energy and power densities, together with outstanding cycling stability. Importantly, the integration of the AIHSC with glucose and pressure sensors highlights its practical potential as a multifunctional, wearable health-monitoring platform. Thus, the core novelty of this study lies in the synergistic combination of material design and device architecture to realize high-performance and multifunctional energy storage in real-world wearable electronics.

2 Results and discussion

Wearable health monitoring sensors require highly efficient and flexible energy storage devices. To meet this demand, we have developed a band-aid-based flexible energy storage device that seamlessly integrates with wearable sensors while ensuring electrochemical stability through a Nb_2C/$MoSe_2$ AIHSC framework. AIHSCs were fabricated using a band-aid coated with Nb_2C/$MoSe_2$ as the cathode, activated carbon as the anode, and a PVA/$(NH_4)_2SO_4$ gel electrolyte. From Fig. 1A Nb_2C exhibits an accordion-like layered structure, which is typical of multilayer Nb_2C. Fig. S1 shows the SEM images of pristine MoS_2 (a) and $MoSe_2$ (b). MoS_2 shows stacked, platelet-like nanosheets with an agglomerated morphology, while $MoSe_2$ exhibits larger, smoother, and more loosely packed lamellae with visible interflake porosity. Fig. 1B and C display an interfacial integration and partial accommodation of MoS_2 and $MoSe_2$ petal-like morphologies in the multilayered structure of Nb_2C. This result confirms that the existence of MoS_2 and $MoSe_2$ could effectively inhibit the stacking of the MXene sheets and enhance the charge transport, thus improving the corresponding electrochemical performance. The EDX spectrum for the Nb_2C/$MoSe_2$ sample in Fig. 1D confirms the presence of Nb, Se, C, O, and Mo. The discovered elements of these materials demonstrate a good synthesis and a homogeneous mixing of $MoSe_2$ nanoplatelets and Nb_2C nanoparticles, which is consistent with the SEM results.

Fig. 1E shows the X-ray diffraction patterns of Nb_2C, Nb_2C/$MoSe_2$, and Nb_2C/MoS_2. Due to the Nb–Al bond breaking, which widened the interlayer gap, a broader characteristic peak, represented by the Nb_2C MXenes' (002) plane, appeared at 9.04°.

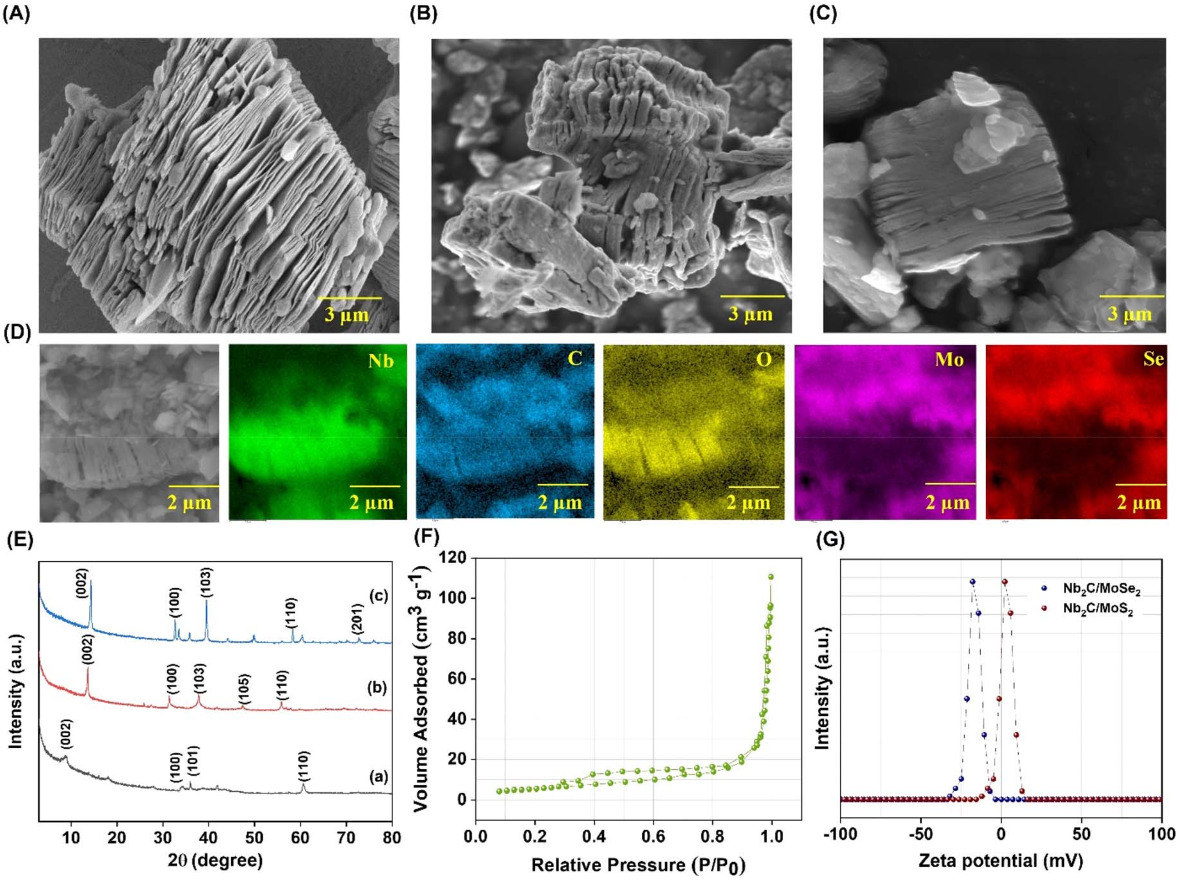

Fig. 1 Structural and morphological characterization: (A) SEM images of Nb_2C MXenes; (B) Nb_2C/MoS_2; (C) $Nb_2C/MoSe_2$; (D) elemental mapping from the SEM image of the $Nb_2C/MoSe_2$ nanocomposite. (E) XRD spectra of (a) Nb_2C MXenes; (b) $Nb_2C/MoSe_2$; (c) Nb_2C/MoS_2. (F) Surface area analysis of the $Nb_2C/MoSe_2$ nanocomposite. (G) Zeta potential measurement of $Nb_2C/MoSe_2$ and Nb_2C/MoS_2 nanocomposites.

The XRD pattern of Nb_2C shows a relatively low-intensity (002) reflection, which is characteristic of multilayer MXenes and indicates that complete delamination did not occur. This observation is consistent with prior reports.[29] In our study, no additional intercalation or exfoliation steps were applied; therefore, the Nb_2C used is confirmed to be multilayer MXenes, exhibiting the stacked, accordion-like morphology seen in SEM (Fig. 1A). Additionally, three diffraction peaks were observed at 60°, 39.1°, and 33.8°. These align with the crystallographic planes (100), (101), and (110) of hexagonal Nb_2C MXenes (JCPDS no. 00-015-0127).[2] After $MoSe_2$ is added to the MXene surface, the (002) peak position moves to the right side, indicating that the order that operates between the Nb_2C layers is disrupted. The diffraction peaks were found at angles of $2\theta = 12.7°$, 31.9°, 38.2°, and 56.4°, which correspond to the planes (002), (100), (103), and (110), respectively, based on the XRD pattern. The hexagonal structure of $MoSe_2$ is linked to the observed peaks, and this structure matches the conventional powder diffraction pattern of $MoSe_2$ from JCPDS card no. 87-2419.27.[30] According to ICCD 03-065-0160, MoS_2 displays a broad peak ($2\theta = 14.08°$) connected to the (002) plane in the case of Nb_2C/MoS_2. Four other diffraction peaks were also seen at $2\theta = 33°$, 39°, 58°, and 62°, which were attributed to the (100), (103), (110) and (201) planes, respectively.[31,32] The confinement of MoS_2 between the MXene layers was confirmed by low-intensity peaks at 2θ angles of 33°, 39°, and 57°.[33] Nevertheless, because of the nanostructured MoS_2 creation linked to Nb_2C, MoS_2 peaks such as (002) at 14.08° and (100) at 33° were overlapped by the Nb_2C/MoS_2 pattern. When the XRD patterns of Nb_2C and Nb_2C/MoS_2 were compared, the (002) peak was discovered to be displaced to the right, indicating that MXenes had a greater interplanar spacing because MoS_2 was restricted between their layers. The XRD patterns show that the full width at half maximum (FWHM) of the $Nb_2C/MoSe_2$ and Nb_2C/MoS_2 lattices has increased with the incorporation of $MoSe_2$ and MoS_2. The $Nb_2C/MoSe_2$ sample has an average crystallite size of 39 nm, while the Nb_2C/MoS_2 sample has a crystallite size of 47 nm. The normal crystallite size for both the $MoSe_2$ and MoS_2 phases has shrunk with the addition of Nb_2C, which contributes to good electrochemical performance. Although the $Nb_2C/MoSe_2$ sample has a smaller crystallite size (39 nm) compared to Nb_2C/MoS_2 (47 nm), as indicated by its broader FWHM, this suggests more disorder and exfoliation in the $MoSe_2$ sample. This finding is another confirmation that $MoSe_2$ more effectively disrupts the interlayer order, suggesting better prevention of restacking.

For $Nb_2C/MoSe_2$, N_2 adsorption–desorption experiments are carried out, resulting in BET surface areas of 127 $m^2\ g^{-1}$, respectively (Fig. 1F). The pristine Nb_2C and Nb_2C/MoS_2

nanocomposite are shown in Fig. S2. The $Nb_2C/MoSe_2$ composite isotherms suggest the existence of a micro mesoporous structure. Together with the interlayer aggregation of $MoSe_2$, the layers of Nb_2C MXenes offer a greater volume and a more accessible specific surface area. These elements help to lower the initial resistance and increase the specific capacitance. The overall electrochemical behavior is further enhanced by the presence of effective ion-transfer channels, which are indicated by the combination of micro and mesopores. As a result of stacking, $Nb_2C/MoSe_2$ possessed a comparatively large surface area compared to Nb_2C/MoS_2. Furthermore, Table S1 (SI) provides the pore size and the pore volume distribution. Zeta potential analysis was used to ascertain charge at the surface, as illustrated in Fig. 1G. Nanosuspension stability is represented by a greater negative or positive zeta potential, which results from electrostatic repulsive forces between nanoparticles.[34] The input of repulsive forces, primarily van der Waals forces, causes nanoparticles to aggregate at the lowest zeta potential value. The zeta potential value of −9.3 mV for the $Nb_2C/MoSe_2$ nanocomposite indicates low stability, while the zeta potential value of −23 mV for the Nb_2C/MoS_2 nanocomposite suggests higher stability. This indicates that the $Nb_2C/MoSe_2$ is significantly more agglomerated, suggesting that van der Waals forces caused the intercalation of $MoSe_2$ nanoplatelets and Nb_2C nanosheets.

The electrochemical performance of pristine Nb_2C, $MoSe_2$ and MoS_2 electrodes was tested in a half-cell assembly, which consisted of a working electrode, reference electrode, and counter electrode using three different electrolytes (Fig. S3). Fig. S3A shows the cyclic voltammogram (CV) curves of the Nb_2C electrode at a scan rate of 30 mV s^{-1} across the potential window for the three different electrolytes (1 M $(NH_4)_2SO_4$, 1 M $ZnSO_4$, and 1 M Na_2SO_4). From the CV curves, symmetric charge–discharge curves are observed, which prove the good reversibility and capacitive behavior of the electrode. Fig. S3B shows the CV curves of the $MoSe_2$ electrode at a scan rate of 30 mV s^{-1}, and the curves exhibit a pair of prominent redox peaks. This results in the battery-type behaviour of the $MoSe_2$ electrode. In the case of the MoS_2 electrode, the CV curves in all the electrolytes are symmetric, which suggests that the electrode has excellent reversibility (Fig. S3C). Fig. S3D–F shows the galvanostatic charge–discharge curves of pristine Nb_2C, $MoSe_2$ and MoS_2 electrodes at all three electrolytes. The specific capacitance of each electrode is shown in Table S2.

The electrochemical behavior of the $Nb_2C/MoSe_2$ and Nb_2C/MoS_2 electrodes was also investigated using a half cell consisting of a working electrode ($Nb_2C/MoSe_2$ and Nb_2C/MoS_2), reference electrode (Ag/AgCl), and counter electrode (platinum wire) in three different electrolytes (1 M $(NH_4)_2SO_4$, 1 M $ZnSO_4$, and 1 M Na_2SO_4). Fig. 2A depicts the CV curves recorded at a 30 mV s^{-1} scan rate for the $Nb_2C/MoSe_2$ electrode with the potential window recorded from −0.4 to 0.4 V, 0.0 to 1.0 V, and 0.0 to 1.0 V for 1 M Na_2SO_4, 1 M $(NH_4)_2SO_4$ and 1 M $ZnSO_4$, respectively. All CV curves show quasi-rectangular shapes. CV curve (b) shows the highest current response, indicating it has the highest capacitance among the three. Curve (a) has the lowest current response, suggesting the lowest capacitance. The curves are not perfectly rectangular, indicating the presence of both electric double-layer capacitance (EDLC) and some faradaic (pseudocapacitive) contributions. Fig. 2B presents the GCD data of $Nb_2C/MoSe_2$ at three different electrolytes, and the obtained potential window well matched with the potential obtained from CV analysis. All curves exhibit a nearly symmetric triangular shape, which is typical for capacitive behavior (ideal supercapacitor). This symmetry indicates good reversibility and low internal resistance. In the case of GCD, curve (b) has the longest discharge time, which means it stored and delivered the most charge and eventually attained the highest specific capacitance. Curve (c) has a moderate discharge time, and curve (a) has the shortest discharge time and has the lowest capacitance. The symmetrical charge–discharge curves suggest good capacitive behavior, and possibly a mix of EDLC and pseudocapacitance. The specific capacitance contribution of each different electrolyte is shown in Fig. 2C. A greater specific capacitance of 252 F g^{-1} at 1 A g^{-1} was found for $Nb_2C/MoSe_2$ electrode in 1 M $(NH_4)_2SO_4$ than in 1 M $ZnSO_4$ (82 F g^{-1}) and 1 M Na_2SO_4 (38 F g^{-1}). In the $Nb_2C/MoSe_2$ system, compared to the storage properties of various metal ions (Na^+ and Zn^{2+}), the specific capacitance of nonmetal NH_4^+ is noticeably higher. NH_4^+ ions have a smaller hydrated radius than Na^+ and Zn^{2+}, which allows easier and faster ion diffusion into the electrode's pores. Also, NH_4^+ ions can behave similarly to protons (H^+) and engage in pseudo-capacitive redox reactions, contributing additional faradaic charge storage.

This hybrid mechanism (EDLC + pseudocapacitance) enhances total capacitance. This improves charge storage efficiency, particularly in porous materials. $NH_4^+ < Na^+ < Zn^{2+}$ is the general trend of hydrated ionic radii in aqueous electrolytes, which correlates with the observed capacitance: smaller hydrated ions diffuse more easily into electrode pores, leading to faster ion transport and higher rate capability. This is because a smaller charge carrier typically results in faster ion diffusion and, thus, better rate capability.[35] The superior performance of NH_4^+ over Na^+ and Zn^{2+} arises from its smaller hydrated ionic radius, which facilitates rapid diffusion and efficient pore utilization. Moreover, NH_4^+ ions engage in hydrogen-bonding interactions with the $Nb_2C/MoSe_2$ electrode, stabilizing the electrode/electrolyte interface and enhancing long-term cycling stability. In contrast, Na^+ and Zn^{2+} ions exhibit slower diffusion and weaker interfacial interactions, resulting in lower specific capacitance and poorer rate capability. Fig. 2D displays the scan speeds of the CV curves for $Nb_2C/MoSe_2$ electrode in 1 M $(NH_4)_2SO_4$ within a potential range of 0.0 to 1.0 V. The CV curves suggest that the electrode has excellent reversibility. CV curves retain shape but get distorted at higher scan rates, which is typical due to increased resistance and limited ion diffusion. The increasing current response with scan rate suggests good rate capability. Some deviation from the ideal rectangular shape indicates a combination of capacitive and faradaic behavior. The wearable $Nb_2C/MoSe_2$ performance in 1 M $(NH_4)_2SO_4$ electrolytes at different current densities was assessed by analysing GCD data (Fig. 2E). The triangular shape of the GCD curve exhibits good reversibility, which was well agreed with the performance observed

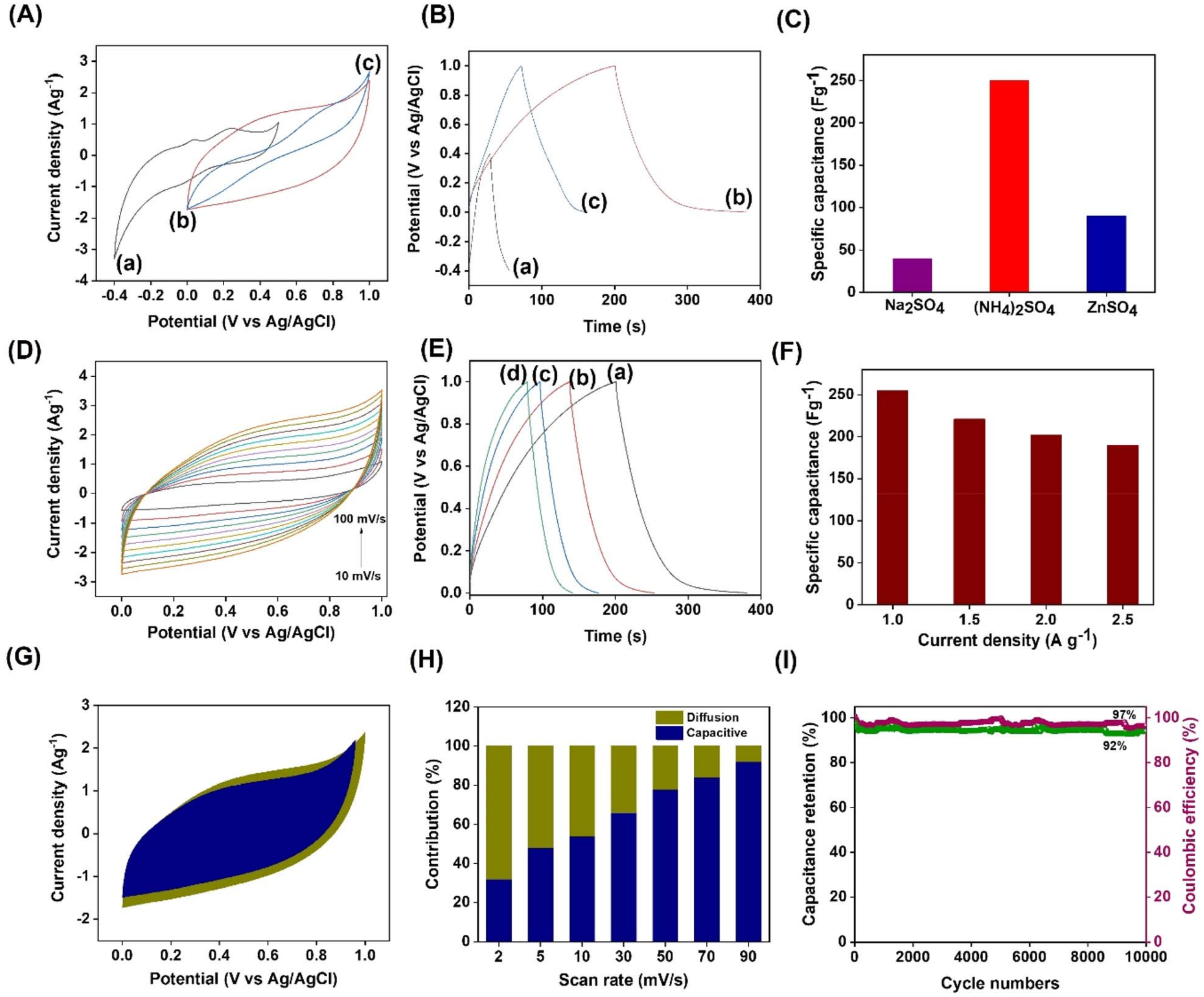

Fig. 2 Electrochemical performances of the $Nb_2C/MoSe_2$ flexible electrode: (A) comparison of cyclic voltammograms (30 mV s^{-1}) of (a) 1 M Na_2SO_4; (b) 1 M $(NH_4)_2SO_4$; (c) 1 M $ZnSO_4$. (B) Galvanostatic charge–discharge curves of (a) 1 M Na_2SO_4; (b) 1 M $(NH_4)_2SO_4$; (c) 1 M $ZnSO_4$. (C) Comparison bar graph of electrolytes *versus* specific capacitance. (D) Cyclic voltammograms of $Nb_2C/MoSe_2$ at various scan rates. (E) Galvanostatic charge–discharge curves of $Nb_2C/MoSe_2$ at different current densities: (a) 1 A g^{-1}; (b) 1.5 A g^{-1}; (c) 2 A g^{-1}; (d) 2.5 A g^{-1}. (F) Graph of specific capacitance *versus* current density. (G) CV curve of total capacitive and diffusion-controlled contribution at 50 mV s^{-1}. (H) Capacitive and diffusion-controlled contribution calculated at different scan rates of the $Nb_2C/MoSe_2$ electrode. (I) Stability performance of $Nb_2C/MoSe_2$ electrodes for 10 000 cycles at 5 A g^{-1}.

from CV curves and a quick ion transport mechanism. As the current density increases from (a) to (d), the discharge time decreases, leading to lower specific capacitance at higher currents. Curve (a) has the longest discharge and highest capacitance at the lowest current density. The curves are still fairly linear and symmetric, indicating stable charge/discharge performance. The specific capacitance (C_{sp}) of $Nb_2C/MoSe_2$ at 1 M $(NH_4)_2SO_4$ is gradually decreased at varying current densities (Fig. 2F). Additionally, it is observed that the discharge time decreases as the current density increases. Rapid ion transport at the electrode–electrolyte interface and inadequate use of the effective surface area are the causes of this phenomenon. Fig. 2G compares the total capacitive and diffusion control of the $Nb_2C/MoSe_2$ electrode at a scan rate of 50 mV s^{-1}. Using the power law (SI), diffusion-controlled or surface/capacitive-controlled charge storage is predicted.[36] The contribution ratio of the response mechanism at various scan rates was computed using Dunn's method (Fig. 2H).[37,38]

The sandwiched $Nb_2C/MoSe_2$ electrode's diffusion-controlled and capacitive contributions are displayed in the bar diagram at various scan speeds (2, 5, 10, 30, 50, 70, and 90 mV s^{-1}). These correspond to 31%, 46%, 53%, 65%, 77%, 83%, and 91% capacitive contributions. The cycling stability of the $Nb_2C/MoSe_2$ hybrid flexible electrode is demonstrated by the GCD test in Fig. 2I for 10 000 charge and discharge cycles at a current density of 5 A g^{-1}. The capacitance of the $Nb_2C/MoSe_2$ electrode decreases by 8% after 10 000 cycles. The electrode exhibits exceptional electrochemical robustness by maintaining a 92% capacitance retention rate. Coulombic efficiency stays near 97%, showing high reversibility and minimal degradation over time.

Similarly, Fig. 3A and B depict the CV curves recorded at a 30 mV s^{-1} scan rate and GCD data of the Nb_2C/MoS_2 electrode within an operating potential range observed from 0.0 to 1.0 V, 0.0 to 1.0 V, and 0.0 to 0.8 V for 1 M Na_2SO_4, 1 M $(NH_4)_2SO_4$ and 1 M $ZnSO_4$, respectively. The non-ideal CV shape suggests a combination of electric double-layer capacitance and pseudocapacitance. The symmetric charge–discharge profiles imply good reversibility and low internal resistance. Fig. 3C displays the specific capacitance contribution of the electrolytes. Among the three electrolytes, Nb_2C/MoS_2 in 1 M $(NH_4)_2SO_4$ exhibits very high specific capacitance. Electrolytes containing NH_4^+ have a specific capacitance of 110 F g^{-1}, higher than that of Zn^{2+} (50 F g^{-1}) and Na^+ (28 F g^{-1}). NH_4^+ can engage in pseudocapacitive redox reactions due to proton-like behavior. Higher ionic conductivity and efficient interaction with the electrode surface facilitate both EDLC and faradaic contributions, maximizing charge storage. The CV scan rates for the Nb_2C/MoS_2 electrode in 1 M $(NH_4)_2SO_4$ with a potential range of 0.0 to 1.0 V are shown in Fig. 3D. The as-fabricated Nb_2C/MoS_2 electrode displays electric double-layer performance. Increased current with scan rate confirms good rate capability. Slight distortion of curves at higher scan rates is typical due to ion diffusion limits but still maintains a stable shape, indicating fast charge propagation and stable electrochemical behavior. The wearable Nb_2C/MoS_2 electrochemical performance in 1 M $(NH_4)_2SO_4$ electrolytes at various current densities was analyzed (Fig. 3E). The linear charge–discharge curve exhibits exceptional EDLC behavior and reversibility,

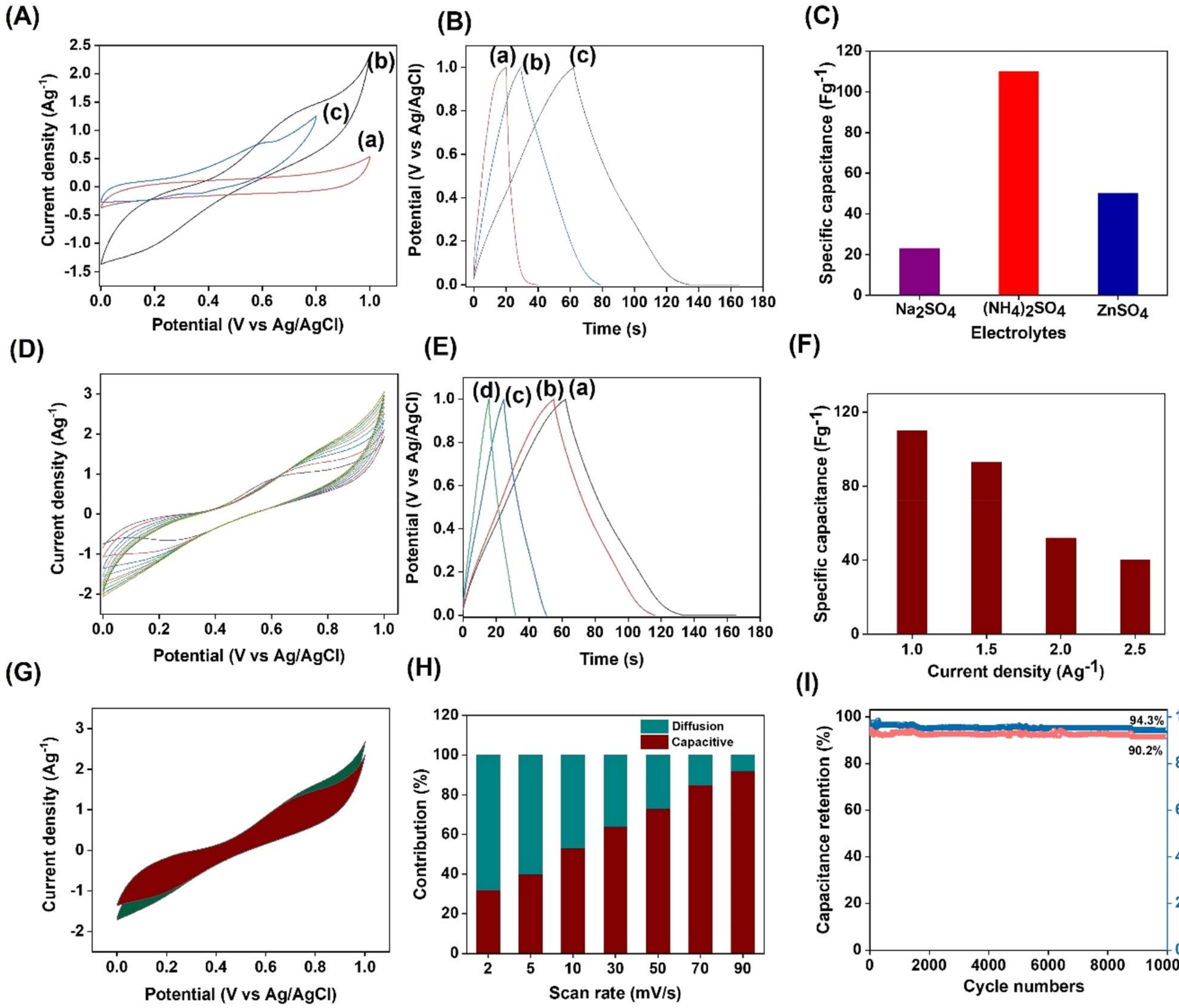

Fig. 3 Electrochemical performances of the Nb_2C/MoS_2 flexible electrode: (A) comparison of cyclic voltammograms (30 mV s^{-1}) of (a) 1 M Na_2SO_4; (b) 1 M $(NH_4)_2SO_4$; (c) 1 M $ZnSO_4$. (B) Galvanostatic charge–discharge curves of (a) 1 M Na_2SO_4; (b) 1 M $(NH_4)_2SO_4$; (c) 1 M $ZnSO_4$. (C) Comparison bar graph of electrolytes *versus* specific capacitance. (D) Cyclic voltammograms of Nb_2C/MoS_2 at various scan rates. (E) Galvanostatic charge–discharge curves of Nb_2C/MoS_2 at different current densities: (a) 1 A g^{-1}; (b) 1.5 A g^{-1}; (c) 2 A g^{-1}; (d) 2.5 A g^{-1}. (F) Graph of specific capacitance *versus* current density. (G) CV curve of total capacitive and diffusion-controlled contribution at 50 mV s^{-1}. (H) Capacitive and diffusion-controlled contribution calculated at different scan rates of the Nb_2C/MoS_2 electrode. (I) Stability performance of Nb_2C/MoS_2 electrodes for 10 000 cycles at 5 A g^{-1}.

which was well agreed with the performance observed from CV curves, indicating good electrochemical performance and a quick ion transport mechanism. Specific capacitance drops at higher currents due to incomplete ion diffusion into porous structures, leaving less time for redox reactions to contribute at high current densities. The specific capacitance (C_{sp}) of Nb_2C/MoS_2 in 1 M $(NH_4)_2SO_4$ is gradually decreased at varying current densities (Fig. 3F). Fig. 3G compares the diffusion-controlled and total capacitance of the Nb_2C/MoS_2 electrode at a scan rate of 50 mV s^{-1}. The faradaic mechanism is observed to dominate the electrode's capacitance at low scan rates. The contribution of intercalation/deintercalation decreases as the scan rate increases, while the non-diffusion controlled capacitive contribution begins to increase.

In Fig. 3H, the bar diagram shows the diffusion-controlled and capacitive contributions of the fabricated Nb_2C/MoS_2 electrode at different scan rates (2, 5, 10, 30, 50, 70, and, 90 mV s^{-1}). The corresponding capacitive contributions are 31%, 39%, 52%, 63%, 72%, 84%, and 91%, respectively. Fig. 3I shows the cycling stability of Nb_2C/MoS_2 in 1 M $(NH_4)_2SO_4$ over 10 000 cycles at a current density of 5 A g^{-1}. The electrode shows a 15% decline in specific capacitance after 10 000 cycles, demonstrating high reversibility and minimal structural degradation over extended operation. Therefore, the $Nb_2C/MoSe_2$ electrode's comparatively intact sheet structure in the NH_4^+ electrolyte suggests that NH_4^+ and the electrode form a hydrogen bond, which improves NH_4^+ adsorption onto the electrode material and contributes to the exceptional cycling stability.[39] Additionally, NH_4^+ exhibits superior electrochemical stability, ion migration rate, and hydrogen bonding interactions with the $Nb_2C/MoSe_2$ electrode compared to Nb_2C/MoS_2, giving supercapacitors a very high specific capacitance and noticeable cycling stability.

Moreover, the different electrochemical behavior of $Nb_2C/MoSe_2$ and Nb_2C/MoS_2 is due to $MoSe_2$ being more redox-active, having lower electronegativity of Se, better electronic conductivity, and different redox potentials and ion intercalation behavior. Therefore, $MoSe_2$ may reach its redox limits or decompose earlier/later, requiring a different optimized potential window to accurately capture its behavior in each electrolyte. In contrast, MoS_2 may operate stably within a single common window across all three electrolytes, especially if it exhibits more capacitive (surface-controlled) rather than battery-type (redox) behavior. This comparison aims to investigate how replacing sulfur (MoS_2) with selenium ($MoSe_2$) affects the electrochemical performance of the Nb_2C layered structure, due to differences in conductivity, interlayer spacing, and redox behavior. The $Nb_2C/MoSe_2$ composite demonstrated superior electrochemical performance compared to Nb_2C/MoS_2. This improvement is attributed to the higher electrical conductivity and larger interlayer spacing of $MoSe_2$, which facilitate faster ion diffusion and charge transfer. Moreover, $MoSe_2$ forms more favorable interfaces with Nb_2C, enhancing electron mobility at each layered junction. These advantages are reflected in the CV and GCD profiles, which show higher current response, improved capacitance, and lower internal resistance for $MoSe_2$-based composites. To further validate the $Nb_2C/MoSe_2$ electrode performance, electrochemical impedance analysis of all three electrolytes was carried out, as shown in Fig. S4. The 1 M Na_2SO_4 electrolyte exhibits maximum resistance behaviour, indicated by the largest semicircle (highest $R_{ct} = 20\ \Omega$). The less steep line in the low-frequency region exhibits poor capacitive behavior because of the presence of Na^+, which has a relatively large hydrated radius, causing sluggish ion transport and poor wettability or weaker interaction with the electrode. In the case of 1 M $ZnSO_4$, it exhibits low $R_{ct} = 9\ \Omega$, but is limited by diffusion kinetics even though the Zn^{2+} has a high charge density (strong attraction to the electrode). However, it has a larger hydrated radius and slower mobility than NH_4^+. The lowest total resistance (lowest real Z' value) is observed for 1 M $(NH_4)_2SO_4$, which exhibits a very small semicircle (very low $R_{ct} = 4\ \Omega$), and the steep linear region exhibits the excellent capacitive behavior (closer to vertical). Low internal resistance facilitates fast charge transfer and efficient ion transport. The EIS analysis confirms that $(NH_4)_2SO_4$ offers the lowest impedance, highest ion mobility, and fastest charge transfer, making it the most efficient electrolyte among the three electrolytes.

A wearable ammonium ion supercapacitor (AIHSC) device was constructed with PVA/$(NH_4)_2SO_4$ gel electrolyte. The flexible $Nb_2C/MoSe_2\|AC$ scheme is shown in Fig. 4A. Fig. 4B and C illustrate CV curves over various scan rates and the GCD with various current densities for the fabricated band-aid AIHSC. The CV curves exhibit clear symmetric charging and discharging curves at all scan rates and deliver the ideal capacitive behavior of $Nb_2C/MoSe_2\|AC$. The maximum specific capacitance of 120 F g^{-1} at a current density of 1 A g^{-1}, which is two times lower than the value observed in the 1 M $(NH_4)_2SO_4$ aqueous electrolyte because of the PVA/$(NH_4)_2SO_4$ electrolyte's lower ionic coefficient and the inadequate transport of ions toward the interface between the electrolyte and the active material. Minimal voltage drop and linear slopes indicate low internal resistance and good rate performance. The specific capacitance of the fabricated device at different current densities is provided in Fig. 4D, where it decreases linearly. At higher current densities, there is less time for ions to penetrate the deeper pores, reducing capacitance due to the limited usage of the active material. The higher current leads to a significant internal resistance drop ($V = IR$), which reduces the effective discharge voltage window. Capacitance inherently decreases at higher current densities, which is consistent with kinetic limitations. This behavior is commonly observed in hybrid supercapacitors and does not necessarily reflect poor performance but rather is a limitation of ion transport at high rates. Fig. 4E shows the contribution at different scan rates for $Nb_2C/MoSe_2\|AC$, and the capacitive contribution gradually increases from 44%, 49%, 67%, 74%, 84%, and 89% at scan rates of 5, 10, 30, 50, 70, and 90 mV s^{-1}. Slow migration of NH_4^+ ions at low scan rates results in a longer residence period on the electrode surface. CV analysis of the diffusion-controlled and total capacitance of the $Nb_2C/MoSe_2\|AC$ electrode at a scan rate of 50 mV s^{-1} is shown in Fig. 4F, which facilitates the adsorption of NH_4^+ ions on the $Nb_2C/MoSe_2$ electrode surface. Conversely, when the rapid migration of NH_4^+ ions at a high scan rate disrupts the charging and discharging processes of ions on the

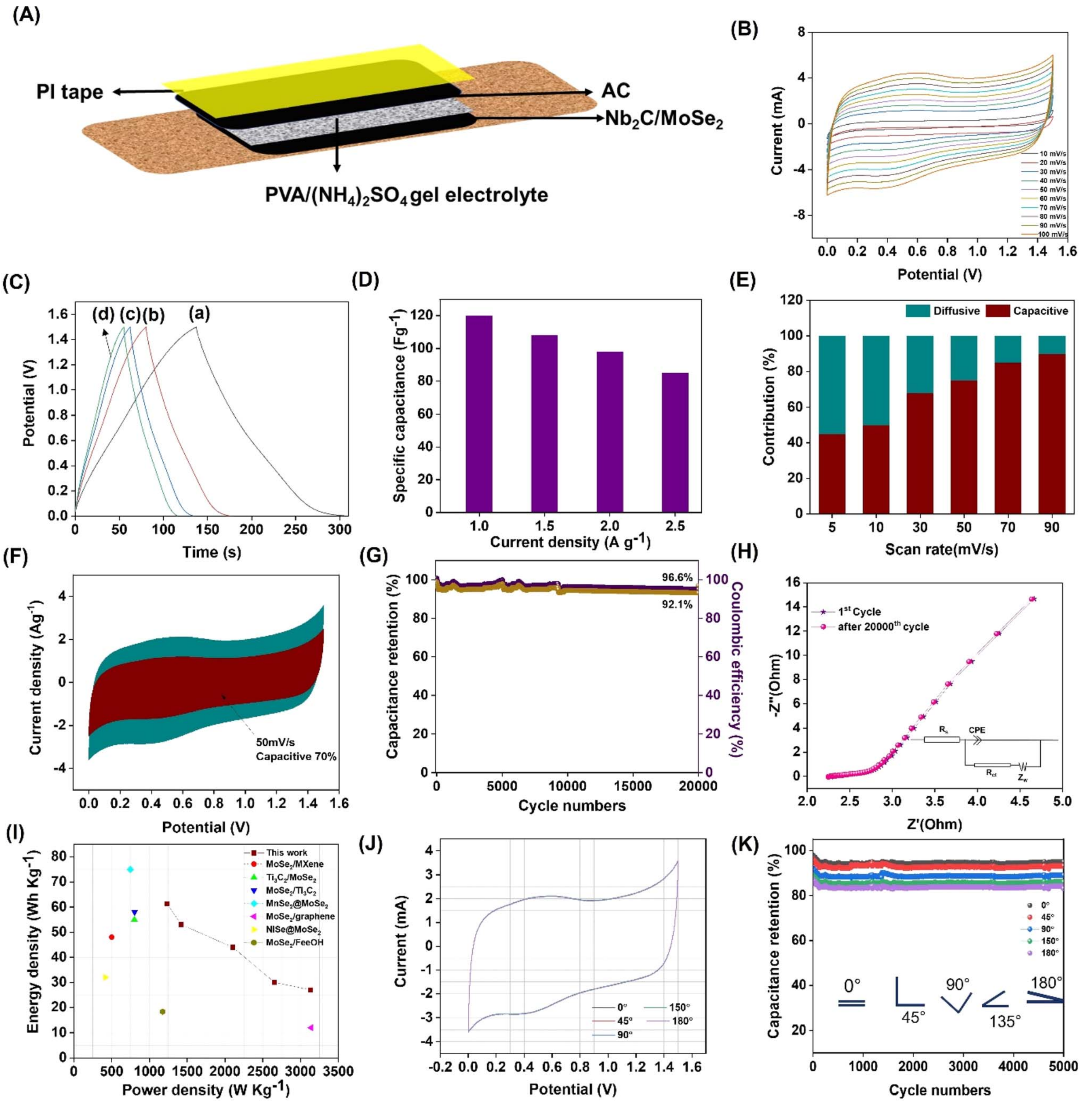

Fig. 4 The electrochemical performance of band-aid-based $Nb_2C/MoSe_2\|AC$ in PVA/$(NH_4)_2SO_4$ nanoparticle gel electrolyte. (A) Schematic illustration of the cell assembly. (B) Cyclic voltammograms at various scan rates. (C) Galvanostatic charge–discharge curves at different current densities: (a) 1 A g^{-1}; (b) 1.5 A g^{-1}; (c) 2.0 A g^{-1}; (d) 2.5 A g^{-1}. (D) Specific capacitance *versus* different current densities. (E and F) Capacitive and diffusion-controlled contributions calculated at various scan rates. (G) Cycling stability and coulombic efficiency (%) (first 10 cycles). (H) Nyquist plot. (I) Ragone plot. (J and K) Mechanical and flexibility study of $Nb_2C/MoSe_2\|AC$ AIHSCs at various bending angles.

surface of the $Nb_2C/MoSe_2$ electrode, it affects the charge transfer between NH_4^+ and $Nb_2C/MoSe_2$. This results in a reaction mechanism where the $Nb_2C/MoSe_2$ electrode is capacitive at high scan rates and pseudocapacitive at low scan rates. A constant current density of 2 A g^{-1} was used to evaluate the cycling stability of the band-aid-based AIHSC across 20 000 cycles (Fig. 4G). After 20 000 cycles, the AIHSC device provides a coulomb efficiency of 96.6% and capacitance retention of 92% respectively. This retains excellent structural stability and low degradation over cycles. After 20 000 charge–discharge cycles, the SEM image and XRD pattern show (Fig. S5) no significant structural or phase changes. This confirms excellent long-term structural stability and durability of the electrode material.

To investigate the charge transfer and electrolyte diffusion at the electrode/electrolyte interface, electrochemical impedance spectroscopy (EIS) was performed on the AIHSC, as shown in

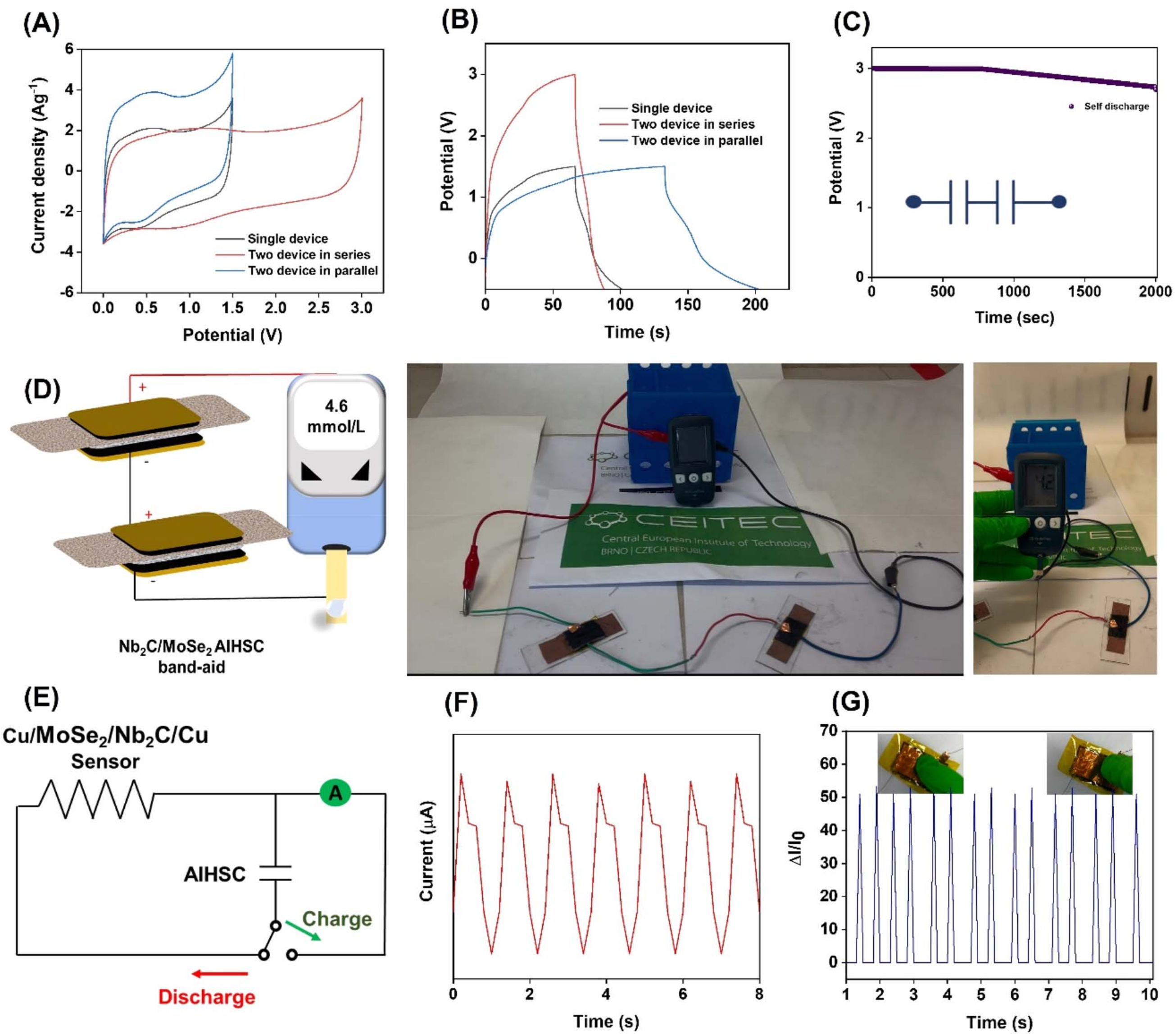

Fig. 5 Wearable band-aid-based Nb$_2$C/MoSe$_2$||AC AIHSC for powering biomonitoring systems: (A) and (B) Cyclic voltammograms and galvanostatic charge–discharge curves of Nb$_2$C/MoSe$_2$||AC in both (a, c) series and (b, d) parallel configurations. (C) Self-discharge curve of two devices connected in series. (D) Schematic illustration and photographs of the powering glucose sensing system with the Nb$_2$C/MoSe$_2$||AC band-aid based AIHSC. (E) Schematic diagram of a self-powered pressure sensor integrated device. (F) Self-powered pressure sensor exhibiting the measurement of radial artery pressure. (G) Real-time monitoring of finger touching.

Fig. 4H. The Nyquist plot displays a small semicircle in the high-frequency region, attributed to the charge-transfer resistance (R_{ct}), and an inclined line in the low-frequency region, associated with Warburg impedance. The Nb$_2$C/MoSe$_2$ electrode exhibits an R_{ct} of approximately 2.6 Ω, reflecting low internal resistance and excellent conductivity. The steep slope in the low-frequency region indicates efficient ion diffusion and nearly ideal capacitive behavior. To further analyze these features, the spectra were fitted using an equivalent circuit composed of series resistance (R_s), charge-transfer resistance (R_{ct}), a constant phase element (CPE), and a Warburg element (W) (inset of Fig. 4H).[40,41] Compared with Nb$_2$C/MoS$_2$, the Nb$_2$C/MoSe$_2$ electrode shows smaller R_s and R_{ct} values, confirming its lower intrinsic resistance, faster charge-transfer kinetics, and superior ion accessibility. Together, these characteristics demonstrate that Nb$_2$C/MoSe$_2$ enables improved charge transport and diffusion pathways, which underpin its enhanced electrochemical performance. The fundamental metrics used to evaluate the performance of supercapacitors are their energy and power densities. The supercapacitor's power density is the ratio of the power it can absorb or disperse to its mass. This indicator assesses a supercapacitor's capacity to quickly release or absorb energy, enabling quick charging, discharging, and a longer lifespan. The AIHSC has a noteworthy energy density of 60 Wh kg^{-1} and a power density of 1236 W kg^{-1}, which is higher than the values found in other materials, as shown in Fig. 4I. However, wearable technology requires a flexible and sturdy device. To evaluate mechanical robustness under different bending angles, the AIHSC retained its capacitive profile at 0°, 45°, 90°, 135°, and 180° (Fig. 4J), indicating minimal distortion of charge-storage kinetics under deformation. Capacity retention after 5000 bending cycles at these angles was 95%, 94%, 90%, 85%, and 82%, respectively (Fig. 4K), evidencing durable electrochemical performance during repeated flexure. Together with the 92% capacitance retention after 20 000 charge–discharge cycles, these results confirm that the electrode/gel–electrolyte interfaces and conductive pathways remain intact during prolonged mechanical actuation.

Two devices coupled in series and parallel at 50 mV s^{-1} have their assembled AIHSC cyclic voltammetry curves shown in Fig. 5A. Interestingly, compared to a single device, the current density of two parallel devices is almost double. In contrast, the potential is increased to 0.0–3.0 V by two serial devices. The charge–discharge period of two devices in parallel is double that of a single device, and the operating potential of two devices is 3.0 V (Fig. 5B). These findings highlight the $Nb_2C/MoSe_2\|AC$ AIHSC's exceptional integrability and consistency. Fig. 5C displays the self-discharge curve of the AIHSC band-aid with devices linked in series. After charging to $\sim$3 V (series of 2 devices), the device shows minimal voltage drop over 2000 s, which indicates good electrolyte stability, low leakage current, and a strong electrode–electrolyte interface. This is important for long-term energy retention in wearable/bioelectronic devices. Fig. 5D displays the serially connected AIHSC powering and testing a glucose meter as proof of concept.

The fabricated ultrasensitive pressure sensor was coupled with the manufactured $Nb_2C/MoSe_2\|AC$ AIHSC to measure real-time arterial pulse pressure. As seen in Fig. 5E, we created a closed circuit by connecting the flexible pressure sensor and supercapacitor vertically to accomplish device integration. To use a self-powered pressure sensor ($Cu\|Nb_2C/MoSe_2\|Cu$) integrated device for monitoring the human body's physiological signals, a PI film was used to secure the flexible pressure sensor and supercapacitor to the skin. The $Nb_2C/MoSe_2\|AC$ device was charged at the electrochemical workstation, and the charged supercapacitor powered the pressure sensor. Additionally, a multimeter was used to measure the change in output current for the applied pressure. As shown in Fig. 5F, the fabricated supercapacitor and pressure sensor were attached to a human wrist for on-body testing. The integrated AIHSC successfully powered the $Cu\|Nb_2C/MoSe_2\|Cu$ pressure sensor, producing stable radial-pulse recordings with a heart rate of $\approx$70 bpm. The current traces exhibited periodic, high-contrast peaks with a steady baseline, confirming stable signal output during wrist movement. In addition, deliberate finger-tapping stimuli generated sharp, reproducible current responses, with variations in peak magnitude and sharpness corresponding to the applied pressure and tapping rate (Fig. 5G). To further evaluate mechanical robustness, the device was mounted on an index finger and tested under fixed-angle and angle-varying bending. As shown in Fig. S6, the pressure sensor delivered consistent current signals in both cases, indicating low hysteresis, good repeatability, and reliable performance under dynamic deformation. The performance of the assembled $MoSe_2$-based supercapacitor for real-time powering of flexible electronic devices with comparable reports is compared in Tables S3 and S4. However, in this work, the full unit, which included a pressure sensor and a supercapacitor, was utilized to measure the arterial pulse pressure of humans in real time. Furthermore, the supercapacitor of the $Nb_2C/MoSe_2\|AC$ AIHSC showed a respectable discharge voltage of 3 V and a charging time of 60 s. Finally, it demonstrates that the fabricated sensor has the advantage of being modular (series/parallel configuration works efficiently), stable (excellent self-discharge performance), practical (capable of powering real-world medical devices like glucose meters), wearable-compatible (supports flexible, on-body biosensing), repeatable and responsive (shows reliable charge/discharge and sensing cycles).

3 Conclusions

In summary, we report a smart wearable band-aid integrating an ammonium-ion hybrid supercapacitor (AIHSC) and pressure sensing, enabled by a $Nb_2C/MoSe_2$ nanocomposite electrode. The $Nb_2C/MoSe_2$ flexible electrode delivers a high specific capacitance of 252 F g^{-1} in 1 M $(NH_4)_2SO_4$ with excellent cycling stability, while the assembled $Nb_2C/MoSe_2\|AC$ AIHSC achieves 120 F g^{-1}, an energy density of 60 Wh kg^{-1}, and a power density of 1236 W kg^{-1}, retaining 92% capacitance after 20 000 cycles. Beyond electrochemical performance, the device exhibits remarkable flexibility and practical applicability by powering glucose and pressure sensors for real-time biosensing. The innovation of this work lies in the synergistic integration of material and device advances: (i) the $Nb_2C/MoSe_2$ nanocomposite electrode that maximizes conductivity, redox activity, and ion transport, and (ii) the first realization of a band-aid-based ammonium-ion supercapacitor as a multifunctional wearable platform. Together, these advances enable high-performance, flexible, and practical energy storage for next-generation health monitoring and sensing applications. Furthermore, the use of a neutral, biocompatible $(NH_4)_2SO_4$ electrolyte ensures both high electrochemical performance and safety advantages over acidic electrolytes, making this system uniquely suited for skin-contact wearable devices.

4 Experimental section

4.1. Materials and chemicals

Ammonium persulfate (99.5%), ammonium sulfate (99.5%), zinc sulfate (99.5%), sodium sulfate (99%), hydrochloric acid, polyvinyl alcohol (PVA, M_w; 8000), lithium fluoride (99.9%), molybdenum sulfide powder (99.9%), and molybdenum selenide powder (99.9%) were purchased from Sigma Aldrich. Niobium aluminium carbide powders were acquired from Hong Kong's Laizhou Kai Ceramic Materials Co. Ltd. Sheets of polyimide were purchased from Fiedler Scientific Instruments in the Czech Republic. A stretchable band-aid was purchased from a local shop in Brno, Czech Republic. All of the compounds were used as analytical reagents without any further purification.

4.2. Synthesis of niobium carbide (Nb_2C)

A 100 ml reaction kettle was first filled with 10 ml of deionized water, and then 30 ml of 12 M HCl was gradually added while being vigorously agitated for 10 minutes. Then, in an ice water bath, 3 g of LiF was gradually added and agitated for 30 minutes to completely react. The reaction kettle was then gradually filled with 2 g of Nb_2AlC powder, which was agitated for 30 minutes. The reactor was then placed in an oven set to 180 °C for twenty-four hours. The MXene solution was washed multiple times by centrifugation in distilled water at 3500 rpm until the pH reached 7. Ultimately, the Nb_2C suspension was freeze-dried to produce MXene powder.[42]

4.3. Fabrication of band-aid-based $Nb_2C/MoSe_2$ electrodes

0.25 g of conductive carbon was initially added into 25 ml of deionized water and stirred for 3 h at 60 °C. Then, the slurry was smoothly coated onto the surface of the band-aid and dried for 8 h at 70 °C. Then, the as-synthesized $Nb_2C/MoSe_2$ and Nb_2C/MoS_2 were coated on the wearable band-aid substrate. The cotton pad in the band-aid was dipped with the prepared PVA/$(NH_4)_2SO_4$ and sandwiched between the activated carbon fabric electrode and the $Nb_2C/MoSe_2$ band-aid electrode. The PI tape was used to seal the device. The device was connected to Cu foil with silver paste for further measurement.

4.4. Integrated glucose monitoring system

The glucose sensor and the $Nb_2C/MoSe_2$ AIHSC band-aid were coupled in series. After dropping the aqueous glucose solution onto the chip, a 5 s waiting period was required. Then an accurate glucose concentration measurement range was displayed on the sensor display.

4.5. Fabrication of the pressure sensor

$Nb_2C/MoSe_2$ was used to create a highly lightweight, flexible, piezoelectric sensor. The $Nb_2C/MoSe_2$ band-aid is positioned between two sheets of copper foil, and copper wires were soldered to the electrodes. To increase its longevity, PI tape was used to enclose the manufactured sensor, which was set up as a $Cu\|Nb_2C/MoSe_2\|Cu$ electrode.

4.6. Materials characterization

Powder X-ray diffraction (XRD) was used to characterize the produced materials using a Rigaku Smart Lab 3kW equipped with an accelerator detector (Cu-Kα radiation, $\lambda = 1.5418$ Å). MIRA with an EDX detector (MIRA3 XMU (MIRA-STAN)) was used to record the surface morphologies and associated elemental mapping. Brunauer–Emmett–Teller (BET) analysis was performed using a Quantachrome instrument. Zeta potential analysis was carried out using a Malvern Zetasizer Nano ZS instrument.

Author contributions

Both M. P. and K. M. conceptualized and designed the idea. K. M. prepared the materials, executed the experiments, and characterized the material. M. P. supervised the work and reviewed the manuscript. The manuscript was written through the contributions of the authors. Both authors have approved the final version of the manuscript.

Conflicts of interest

There is no conflict of interest.

Data availability

Data for this article are available at ZENODO at **https://zenodo.org**.

Supplementary information: (1) Experimental section, figures and tables. (2) Application of the biomonitoring sensor: fabricated AIHSC to power a glucose sensor (Video S1). See DOI: **https://doi.org/10.1039/d5ta06175j**.

Acknowledgements

The work was supported by the ERDF/ESF project TECHSCALE (No. CZ.02.01.01/00/22_008/0004587). This research was co-funded by the European Union under the REFRESH – Research Excellence For Region Sustainability and High-tech Industries project (No. CZ.10.03.01/00/22_003/0000048) *via* the Environment Programme Just Transition. K. M. would like to acknowledge Dr Senthil Nathan for his help in zeta potential measurements and Dr Bindu Kalleshappa for help with sensor experiments. M. P. acknowledges project ANGSTROM for funding. Project ANGSTROM was selected in the Joint Transnational Call 2023 of M-ERA.NET 3, which is an EU-funded network of about 49 funding organisations (Horizon 2020 grant agreement no. 958174). This project "Advancing Supercapacitors with Plasma-designed Multifunctional Hybrid Materials" (no. TQ05000001) is co-financed from the state budget by the Technology Agency of the Czech Republic under the SIGMA Programme within the M-ERA-NET 3 Call 2023. This project/result was funded under the National Recovery Plan from the European Recovery and Resilience Facility.

References

1 G. Pandey, S. Serawat and K. Awasthi, Synergistic Effects of ZnO@NiM′-Layered Double Hydroxide (M′ = Mn, Co, and Fe) Composites on Supercapacitor Performance: A Comparative Evaluation, *ACS Nanosci. Au*, 2024, **4**(6), 399–408, DOI: **10.1021/acsnanoscienceau.4c00029**.

2 Y. Al-Hadeethi, M. W. Iqbal, B. M. Raffah and E. Umar, Synergistic Advancements in Battery-Grade Energy Storage: $Nb_2C/MoTe_2$(PANI) Hybrid Electrode Material as a Enhanced Electrocatalyst for Hydrogen Reduction Reaction, *Electrochim. Acta*, 2024, **508**, 145205, DOI: **10.1016/j.electacta.2024.145205**.

3 X. Gao, P. Wang, Z. Pan, J. P. Claverie and J. Wang, Recent Progress in 2D Layered Double Hydroxides and Their Derivatives for Supercapacitors, *ChemSusChem*, 2019, **13**(6), 1226–1254, DOI: **10.1002/cssc.201902753**.

4 K. Manoharan, R. Sundaram and K. Raman, Expeditious Re-Hydrogenation Kinetics of Ball-Milled Magnesium Hydride (B-MgH_2) Decorated Acid-Treated Halloysite Nanotube (A-HNT)/Polyaniline (PANI) Nanocomposite (B-MgH_2/A-HNT/PANI) for Fuel Cell Applications, *Ionics*, 2023, **29**(7), 2823–2839, DOI: 10.1007/s11581-023-05007-w.

5 Z. Jian, N. Yang, M. Vogel, S. Leith, A. Schulte, H. Schönherr, T. Jiao, W. Zhang, J. Müller, B. Butz and X. Jiang, Flexible Diamond Fibers for High-Energy-Density Zinc-Ion Supercapacitors, *Adv. Energy Mater.*, 2020, **10**(44), 2002202, DOI: 10.1002/aenm.202002202.

6 T. Prasankumar, K. Manoharan, S. Bashir, K. K. Kandiah, K. Ramesh, S. Ramesh, S. Ramesh and V. K. Ramachandaramurthy, Binder-Free Flexible Supercapacitor Utilizing Ni-Doped Biomass-Derived Activated Carbon Embraced with MWCNTs, *Diamond Relat. Mater.*, 2025, **157**, 112473, DOI: 10.1016/j.diamond.2025.112473.

7 X. Chen, Z. Hou, G. Li, W. Yu, Y. Xue, G. Niu, M. Xin, L. Yang, C. Meng and S. Guo, A Laser-Scribed Wearable Strain Sensing System Powered by an Integrated Rechargeable Thin-Film Zinc-Air Battery for a Long-Time Continuous Healthcare Monitoring, *Nano Energy*, 2022, **101**, 107606, DOI: 10.1016/j.nanoen.2022.107606.

8 C. Li, S. Yang, Y. Guo, H. Huang, H. Chen, X. Zuo, Z. Fan, H. Liang and L. Pan, Flexible, Multi-Functional Sensor Based on All-Carbon Sensing Medium with Low Coupling for Ultrahigh-Performance Strain, Temperature and Humidity Sensing, *Chem. Eng. J.*, 2021, **426**, 130364, DOI: 10.1016/j.cej.2021.130364.

9 W. Fu, K. Turcheniuk, O. Naumov, R. Mysyk, F. Wang, M. Liu, D. Kim, X. Ren, A. Magasinski, M. Yu, X. Feng, Z. L. Wang and G. Yushin, Materials and Technologies for Multifunctional, Flexible or Integrated Supercapacitors and Batteries, *Mater. Today*, 2021, **48**, 176–197, DOI: 10.1016/j.mattod.2021.01.026.

10 W. R. de Araujo, C. M. R. Frasson, W. A. Ameku, J. R. Silva, L. Angnes and T. R. L. C. Paixão, Single-Step Reagentless Laser Scribing Fabrication of Electrochemical Paper-Based Analytical Devices, *Angew. Chem., Int. Ed.*, 2017, **56**(47), 15113–15117, DOI: 10.1002/anie.201708527.

11 Y. Wei, X. Li, Y. Wang, T. Hirtz, Z. Guo, Y. Qiao, T. Cui, H. Tian, Y. Yang and T.-L. Ren, Graphene-Based Multifunctional Textile for Sensing and Actuating, *ACS Nano*, 2021, **15**(11), 17738–17747, DOI: 10.1021/acsnano.1c05701.

12 M. Yuan, F. Luo, Z. Wang, J. Yu, H. Li and X. Chen, Smart Wearable Band-Aid Integrated with High-Performance Micro-Supercapacitor, Humidity and Pressure Sensor for Multifunctional Monitoring, *Chem. Eng. J.*, 2023, **453**, 139898, DOI: 10.1016/j.cej.2022.139898.

13 M. Yuan, F. Luo, Y. Rao, Y. Wang, J. Yu, H. Li and X. Chen, Laser Synthesis of Superhydrophilic O/S Co-Doped Porous Graphene Derived from Sodium Lignosulfonate for Enhanced Microsupercapacitors, *J. Power Sources*, 2021, **513**, 230558.

14 J. C. de Haro, E. Tatsi, L. Fagiolari, M. Bonomo, C. Barolo, S. Turri, F. Bella and G. Griffini, Lignin-Based Polymer Electrolyte Membranes for Sustainable Aqueous Dye-Sensitized Solar Cells, *ACS Sustain. Chem. Eng.*, 2021, **9**(25), 8550–8560.

15 F. Fu, D. Yang, W. Zhang, H. Wang and X. Qiu, Green Self-Assembly Synthesis of Porous Lignin-Derived Carbon Quasi-Nanosheets for High-Performance Supercapacitors, *Chem. Eng. J.*, 2020, **392**, 123721, DOI: 10.1016/j.cej.2019.123721.

16 H. S. Shahidani, M. Seifi and M. Bagher Askari, Design of $NiSe_2$@$MoSe_2$ Nanocomposite Anchored on Multi-Walled Carbon Nanotubes as Advanced Supercapacitor Applications, *Inorg. Chem. Commun.*, 2024, **170**, 113218, DOI: 10.1016/j.inoche.2024.113218.

17 M. Tomy, A. Ambika Rajappan, V. Vm and X. Thankappan Suryabai, Emergence of Novel 2D Materials for High-Performance Supercapacitor Electrode Applications: A Brief Review, *Energy Fuels*, 2021, **35**(24), 19881–19900, DOI: 10.1021/acs.energyfuels.1c02743.

18 T. Prasankumar, K. Manoharan, N. K. Farhana, S. Bashir, K. Ramesh, S. Ramesh and V. K. Ramachandaramurthy, Advancements and Approaches in Developing MXene-Based Hybrid Composites for Improved Supercapacitor Electrodes, *Mater. Today Sustain.*, 2024, **28**, 100963, DOI: 10.1016/j.mtsust.2024.100963.

19 M. Arunkumar, K. Nasrin, N. Allwyn, P. Kavinkumar, A. Sivashanmugam and M. Sathish, The Emerging Heteroepitaxial $NiSe_2$/Nb_2C: A Two-In-One Bi-Functional Material Architecture for Electrocatalytic and Supercapattery Application, *Adv. Sustainable Syst.*, 2024, **8**(9), 2400088, DOI: 10.1002/adsu.202400088.

20 A. Tsyganov, A. Shindrov, M. Vikulova, D. Zheleznov, A. Gorokhovsky and N. Gorshkov, Effect of LiCl Electrolyte Concentration on Energy Storage of Supercapacitor with Multilayered $Ti_3C_2T_x$ MXene Electrodes Synthesized by Hydrothermal Etching, *Processes*, 2023, **11**(9), 1–16, DOI: 10.3390/pr11092528.

21 T. Prasankumar, J. Vigneshwaran, S. Abraham and S. P. Jose, 3D Structures of Graphene Oxide and Graphene Analogue MoS_2 with Polypyrrole for Supercapacitor Electrodes, *Mater. Lett.*, 2019, **238**, 121–125, DOI: 10.1016/j.matlet.2018.12.002.

22 F. B. M. Ahmed, D. Khalafallah, M. Zhi and Z. Hong, Porous Nanoframes of Sulfurized NiAl Layered Double Hydroxides and Ternary Bismuth Cerium Sulfide for Supercapacitor Electrodes, *Adv. Compos. Hybrid Mater.*, 2022, **5**(3), 2500–2514.

23 Z. Li, Y. Dall'Agnese, J. Guo, H. Huang, X. Liang and S. Xu, Flexible Freestanding All-MXene Hybrid Films with Enhanced Capacitive Performance for Powering a Flex Sensor, *J. Mater. Chem. A*, 2020, **8**(32), 16649–16660, DOI: 10.1039/D0TA05710J.

24 A. Tsyganov, M. Vikulova, I. Zotov, E. Korotaev, I. Plugin, V. Sysoev, D. Kirilenko, M. Rabchinskii, A. Asoyan, A. Gorokhovsky and N. Gorshkov, Application of $W_{1.33}CT_z$ MXenes Obtained by Hydrothermal Etching as an Additive

to Enhance the Electrochemical Energy Storage Properties of Binder-Free $Ti_3C_2T_x$ MXene Films, *Dalton Trans.*, 2025, **54**(21), 8547–8558, DOI: 10.1039/D5DT00413F.

25 T. Prasankumar, N. Bose, M. Manikandan, N. Mohana Suntharam, K. Manoharan, N. K. Farhana, S. Bashir, K. Ramesh, S. Ramesh and V. K. Ramachandaramurthy, Recent Trends and Challenges in Heteroatom-Rich Carbon-Based Cathode for Zn-Ion Hybrid Supercapacitors, *J. Ind. Eng. Chem.*, 2025, **142**, 157–176, DOI: 10.1016/j.jiec.2024.11.011.

26 X. Wu, Y. Qi, J. J. Hong, Z. Li, A. S. Hernandez and X. Ji, Rocking-Chair Ammonium-Ion Battery: A Highly Reversible Aqueous Energy Storage System, *Angew. Chem., Int. Ed.*, 2017, **56**(42), 13026–13030, DOI: 10.1002/anie.201707473.

27 G. Liang, Y. Wang, Z. Huang, F. Mo, X. Li, Q. Yang, D. Wang, H. Li, S. Chen and C. Zhi, Initiating Hexagonal MoO_3 for Superb-Stable and Fast NH_4^+ Storage Based on Hydrogen Bond Chemistry, *Adv. Mater.*, 2020, **32**(14), 1907802, DOI: 10.1002/adma.201907802.

28 Q. Chen, J. Jin, M. Song, X. Zhang, H. Li, J. Zhang, G. Hou, Y. Tang, L. Mai and L. Zhou, High-Energy Aqueous Ammonium-Ion Hybrid Supercapacitors, *Adv. Mater.*, 2022, **34**(8), 2107992, DOI: 10.1002/adma.202107992.

29 M. Shekhirev, C. E. Shuck, A. Sarycheva and Y. Gogotsi, Characterization of MXenes at Every Step, from Their Precursors to Single Flakes and Assembled Films, *Prog. Mater. Sci.*, 2021, **120**, 100757, DOI: 10.1016/j.pmatsci.2020.100757.

30 H. Peng, J. Zhou, K. Sun, G. Ma, Z. Zhang, E. Feng and Z. Lei, High-Performance Asymmetric Supercapacitor Designed with a Novel $NiSe@MoSe_2$ Nanosheet Array and Nitrogen-Doped Carbon Nanosheet, *ACS Sustain. Chem. Eng.*, 2017, **5**(7), 5951–5963, DOI: 10.1021/acssuschemeng.7b00729.

31 T. Nagarajan, M. Khalid, N. Sridewi, P. Jagadish, S. Shahabuddin, K. Muthoosamy and R. Walvekar, Tribological, Oxidation and Thermal Conductivity Studies of Microwave Synthesised Molybdenum Disulfide (MoS_2) Nanoparticles as Nano-Additives in Diesel Based Engine Oil, *Sci. Rep.*, 2022, **12**(1), 14108, DOI: 10.1038/s41598-022-16026-4.

32 N. Taheri, H. Hashemi, E. Soroush, P. Afsahi and B. Ramezanzadeh, $Ti_3C_2T_x$ MXene/MoS_2 Hybrid Nanocomposites for Synergistic Smart Corrosion Protection of Epoxy Coatings, *J. Colloid Interface Sci.*, 2025, **682**, 894–914, DOI: 10.1016/j.jcis.2024.11.205.

33 M. Chandran, A. Thomas, A. Raveendran, M. Vinoba and M. Bhagiyalakshmi, MoS_2 Confined MXene Heterostructures as Electrode Material for Energy Storage Application, *J. Energy Storage*, 2020, **30**, 101446, DOI: 10.1016/j.est.2020.101446.

34 A. Gopi, A. Vindhyasarumi and K. Yoosaf, Electrostatically Driven Self-Assembly of CdTe Nanoparticles with Organic Chromophores Probed via Ham Effect, *RSC Adv.*, 2015, **5**(59), 47813–47819.

35 S. Dong, W. Shin, H. Jiang, X. Wu, Z. Li, J. Holoubek, W. F. Stickle, B. Key, C. Liu, J. Lu, P. A. Greaney, X. Zhang and X. Ji, Ultra-Fast NH_4^+ Storage: Strong H Bonding between NH_4^+ and Bi-Layered V_2O_5, *Chem*, 2019, **5**(6), 1537–1551, DOI: 10.1016/j.chempr.2019.03.009.

36 K. Manoharan, B. Ramasamy, K. Raman and R. Sundaram, Ultrasonic Assisted Highly Porous PPy/JSAC/IMO [PJ-IMO] Nanocomposite for Hydrogen Fuel Cell and Asymmetric Supercapacitor (PJ-IMO‖JSAC) Applications, *J. Energy Storage*, 2023, **70**, 107931, DOI: 10.1016/j.est.2023.107931.

37 K. Manoharan, R. Sundaram and K. Raman, Preparation and Characterization of Hydrogen Storage Medium (IMO/TPAC) and Asymmetric Supercapacitor (IMO/TPAC‖TPAC) Using Imogolite (IMO) and Biomass Derived Activated Carbon from Tangerine Peel (TPAC) for Renewable Energy Storage Applications, *Int. J. Hydrogen Energy*, 2023, **48**(74), 28694–28711, DOI: 10.1016/j.ijhydene.2023.04.076.

38 B. R. Wiston, S. Tewatia and M. Ashok, Insights into Coprecipitated Cerium Oxide/Hydroxide–Nickel Hydroxide Composite for High Efficacy Supercapacitors, *Mater. Today Sustain.*, 2023, **21**, 100291, DOI: 10.1016/j.mtsust.2022.100291.

39 J. Dai, X. Qi, L. Xia, Q. Xue, L. Luo, X. Wang, C. Yang, D. Li, H. Xie, A. Cabot, L. Dai and Y. Xu, Aqueous Ammonium-Ion Supercapacitors with Unprecedented Energy Density and Stability Enabled by Oxygen Vacancy-Enriched $MoO_3@C$, *Adv. Funct. Mater.*, 2023, **33**(10), 2212440, DOI: 10.1002/adfm.202212440.

40 F. Qi, X. Lu, Y. Wang, H. Zhang, A. Trukhanov and Z. Sun, Fabrication of Hierarchical $MoO_3@Ni_xCo_{2x}(OH)_{6x}$ Core–Shell Arrays on Carbon Cloth as Enhanced-Performance Electrodes for Asymmetric Supercapacitors, *J. Colloid Interface Sci.*, 2022, **607**, 1253–1261, DOI: 10.1016/j.jcis.2021.09.046.

41 Z. Chen, T. Tao, C. Shi, X. Shi, L. Shao, J. Xu and Z. Sun, Tuning the Electronic Structure of Niobium Oxyphosphate/Reduced Graphene Oxide Composites by Vanadium-Doping for High-Performance Na^+ Storage Application, *Carbon Neutralization*, 2025, **4**(3), 1–11, DOI: 10.1002/cnl2.70010.

42 M.-P. Li, C.-B. Zhang, Y.-D. Li, D.-T. Zhang, C.-G. Chang and M.-C. Liu, Insert Organic Molecules into Nb_2C Layers through Hydrogen Bonds towards High-Rate Lithium Ion Storage, *Ionics*, 2022, **28**(11), 5099–5108, DOI: 10.1007/s11581-022-04716-y.